SUPPLEMMENTARY INFORMATION

Harnessing ligand design to optimize primary and self-calibrated luminescent thermometers with field-induced single ion magnet behaviour in Dy^{3+} complexes

Julio Corredoira-Vázquez,[a,b] Cristina González-Barreira,[a] Ana M. García-Deibe,[a] Jesús Sanmartín-Matalobos,[a,c] Miguel A. Hernández-Rodríguez,[†b] Carlos D. S. Brites,[b] Luís D. Carlos[b,*] and Matilde Fondo[a,*]

[a] Departamento de Química Inorgánica, Facultade de Química, Universidade de Santiago de Compostela, 15782 Santiago de Compostela, Spain
[b] Phantom-g, CICECO – Aveiro Institute of Materials, Department of Physics, University of Aveiro, 3810-193 – Aveiro, Portugal
[c] Institute of Materials (iMATUS), Universidade de Santiago de Compostela, 15782 Santiago de Compostela, Spain
† MAHR is currently affiliated with the Departamento de Física, Universidad de La Laguna, Apdo. Correos 456, E-38200 San Cristóbal de La Laguna, Santa Cruz de Tenerife, Spain

Corresponding authors: matilde.fondo@usc.es and lcarlos@ua.pt

Contents

1. Structural Characterization

Table S1. Main bond distances (Å) and angles (°) for 1·2H_2O and 2·$CHCl_3$.

Bond	1·2H_2O	2·$CHCl_3$
Dy1-O21	2.4261(10)	2.4239(19)
Dy1-O22	2.4896(10)	2.398(2)
Dy1-O31	2.3855(10)	2.4349(19)
Dy1-O32	2.4264(10)	2.4588(18)
Dy1-N6	2.5825(12)	2.585(2)
Dy1-N1	2.6414(12)	2.597(2)
Dy1-N2	2.6073(12)	2.613(2)
Dy1-N3	2.6000(12)	2.601(2)
Dy1-N4	2.6497(12)	2.632(2)
Dy1-N5	2.6242(12)	2.613(2)
O21-Dy1-O22	52.96(3)	54.23(7)
O31-Dy1-O32	54.39(3)	53.57(6)
N1-Dy1-N4	179.32(3)	178.13(7)

Table S2. Distances (Å) of the nitrogen and dysprosium atoms form the mean calculated N_6 plane.

Bond	1·2H_2O	2·$CHCl_3$
N1	0.008	0.033
N2	0.496	0.727
N3	0.496	0.763
N4	0.001	0.033
N5	0.501	0.730
N6	0.507	0.760
Dy1	0.012	0.008

Table S3. SHAPE v2.1. Continuous Shape Measures calculation (c) 2013. Electronic Structure Group, Universitat de Barcelona.

Label	Description
DP-10	1 D10h Decagon
EPY-10	2 C9v Enneagonal pyramid
OBPY-10	3 D8h Octagonal bipyramid
PPR-10	4 D5h Pentagonal prism
PAPR-10	5 D5d Pentagonal antiprism
JBCCU-10	6 D4h Bicapped cube J15
JBCSAPR-10	7 D4d Bicapped square antiprism J17
JMBIC-10	8 C2v Metabidiminished icosahedron J62
JATDI-10	9 C3v Augmented tridiminished icosahedron J64
JSPC-10	10 C2v Sphenocorona J87
SDD-10	11 D2 Staggered Dodecahedron (2:6:2)
TD-10	12 C2v Tetradecahedron (2:6:2)
HD-10	13 D4h Hexadecahedron (2:6:2) or (1:4:4:1)

1·$2H_2O$

Structure [ML10]	DP-10	EPY-10	OBPY-10	PPR-10	PAPR-10	JBCCU-10
	36.909,	25.708,	15.151,	11.130,	11.323,	9.044,

JBCSAPR-10	JMBIC-10	JATDI-10	JSPC-10	**SDD-10**	**TD-10**	HD-10
3.856,	6.885,	19.853,	3.140,	**2.451**,	**2.279**,	6.483

2·$CHCl_3$

Structure [ML10]	DP-10	EPY-10	OBPY-10	PPR-10	PAPR-10	JBCCU-10
	36.042,	24.774,	15.126,	12.874,	12.309,	9.262,

JBCSAPR-10	JMBIC-10	JATDI-10	**JSPC-10**	SDD-10	TD-10	HD-10
2.967,	7.570,	19.789,	**3.215**,	5.164,	4.285,	6.814

Table S4. Crystal data and structure refinement for **1**·$2H_2O$ and **2**·$CHCl_3$.

	1·$2H_2O$	**2**·$CHCl_3$
Empirical formula	$C_{22}H_{28}DyN_7O_9$	$C_{25}H_{29}Cl_3DyN_7O_7$
Molecular weight	697.01	808.40
Crystal system	Triclinic	Triclinic
Space group	*P*-1	*P*-1
Wavelength (Å)	0.71073	0.71073
Crystal size (mm^3)	0.150 x 0.080 x 0.040	0.130 x 0.090 x 0.080
Colour, shape	Colourless, needle	Prism, yellow
T (K)	100	100
a (Å)	8.9995(6)	9.8809(5)
b (Å)	11.4256(8)	9.9771(5)
c (Å)	13.7184(10)	16.8451(8)
α (º)	74.867(2)	106.028(2)
β (º)	79.263(2)	102.983(2)
γ (º)	75.331(2)	96.511(2)
Volume ($Å^3$)	1306.33(16)	1527.75(13)
Z	2	2
Absorpt. coef. (mm^{-1})	2.924	2.763
Reflections collected	51079	54786
Independent reflections	6465 [R_{int} = 0.0247]	7577 [R_{int} = 0.0498]
Data / restrains / param.	6465 / 0 / 370	7577 / 0 / 390
Final R indices [$I>2\sigma(I)$]	R_1 = 0.0127; wR_2 = 0.0331	R_1 = 0.0265; wR_2 = 0.0547
R indices (all data)	R_1 = 0.0134; wR_2 = 0.0335	R_1 = 0.0325; wR_2 = 0.0566

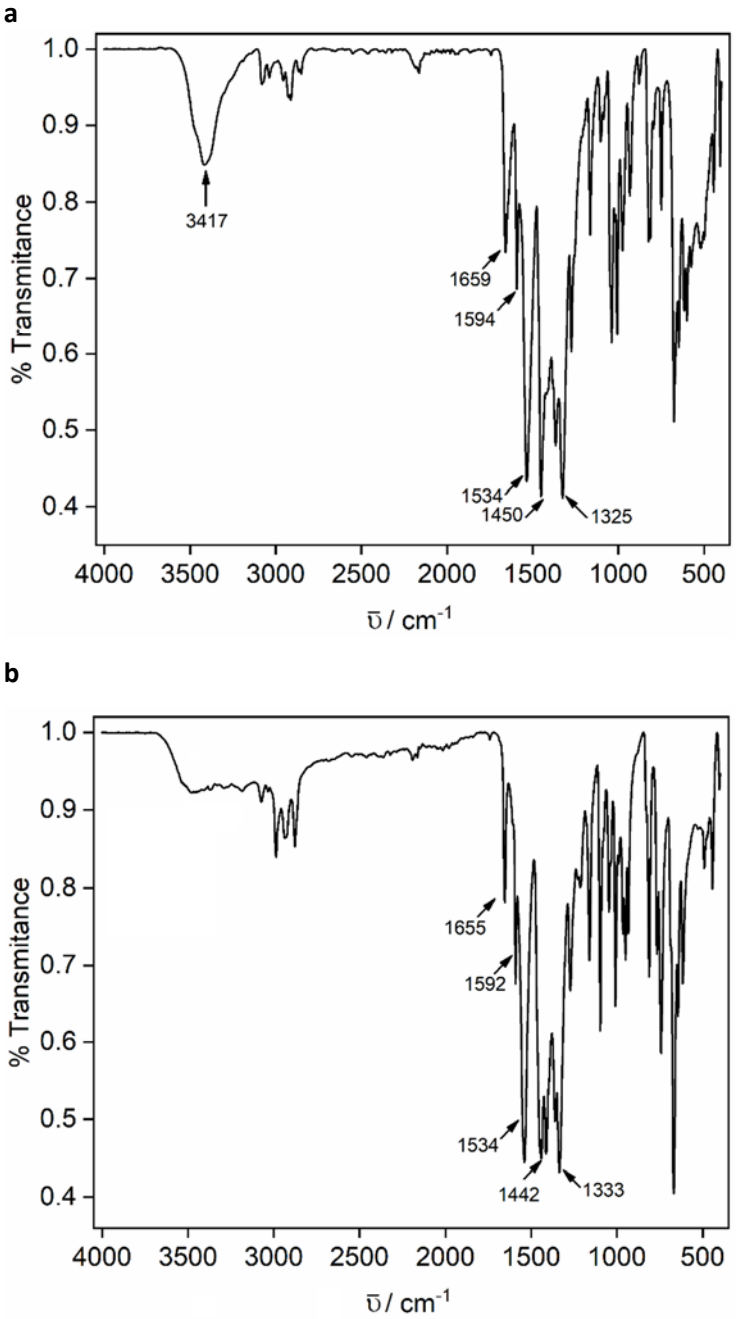

Fig. S1. IR spectra for **1**·2H_2O **(a)** and **2**·$CHCl_3$ **(b)**

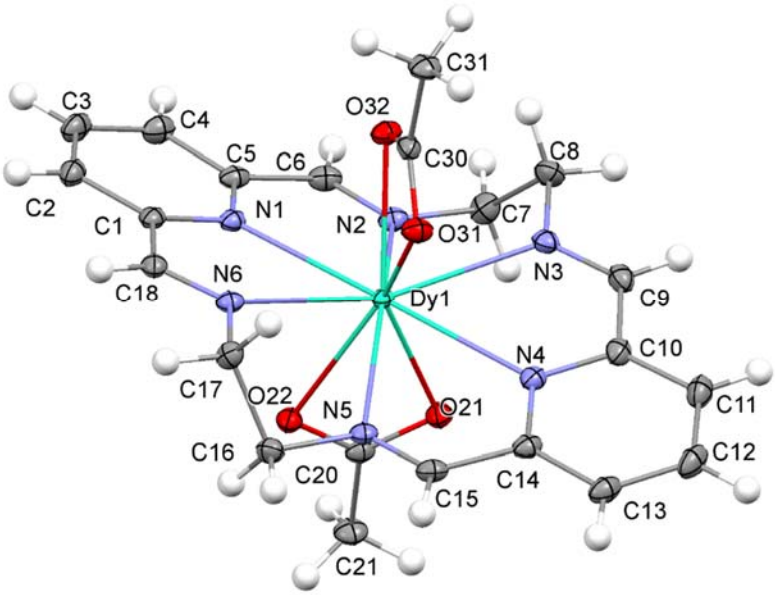

Fig. S2. Ellipsoid diagram (50% probability) for the cation $[Dy(L^{N6en})(OAc)_2]^+$ in $\{[Dy(L^{N6en})(OAc)_2](NO_3)\}\cdot 2H_2O$ (**1**·$2H_2O$).

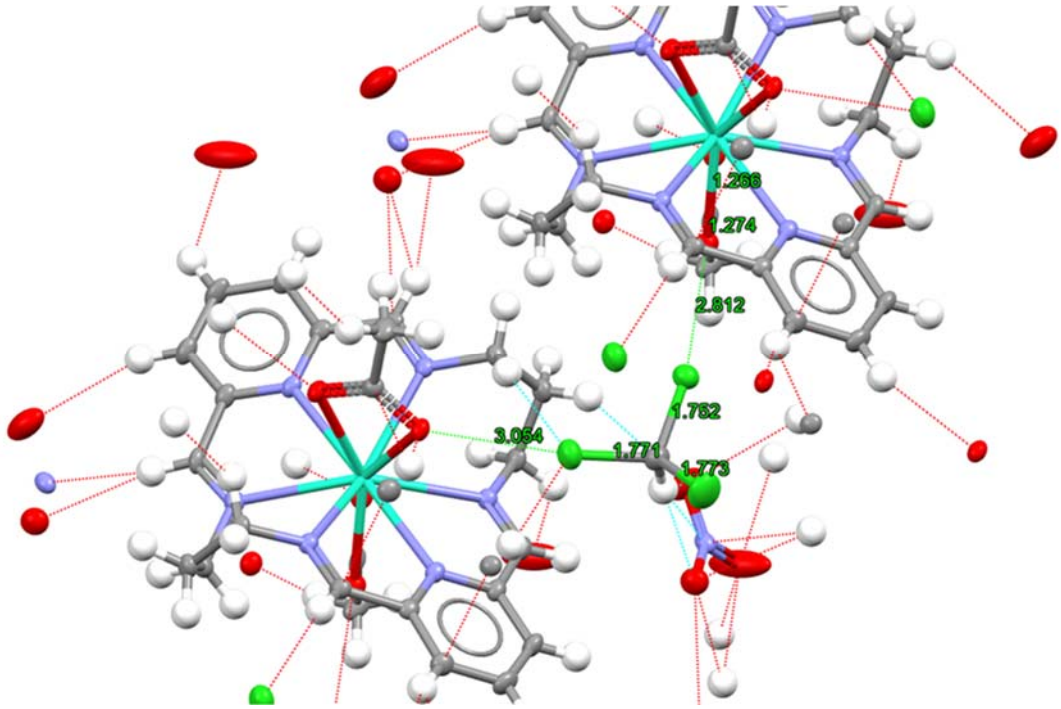

Fig. S3. Portion of the packing diagram, showing the interactions of the solvate with the cations and nitrate anions of the complex $[Dy(L^{N6prop})(OAc)_2](NO_3)$ (**2**). The intermolecular Cl2···O22 distance of 2.81 Å could seem quite short but it has many precedents. Searching in the CSD for other chloroform···oxygen containing groups contacts show that values between 2.8-2.9 Å have been previously reported at least for the following crystal structures in CSD: REFCODE: 1. DADPIK;[1] 2. REFCODE: EGIBII;[2] 3. REFCODE: FANGEI;[3] 4. REFCODE: GALDUU;[4] 5. REFCODE: HIVPUZ;[5] REFCODE: IVUNUI;[6] 7. REFCODE: IWAPOO: Kai Wei, CSD Communication (Private Communication), 2021; 8. REFCODE: MARGEU;[7] 9. REFCODE: NELPOK;[8] 10. REFCODE: TIXXUV01;[9] 11. REFCODE: UVEVOJ;[10] 12. REFCODE: VEFKEY;[11] 13. REFCODE: ZIBWUE;[12] 14. REFCODE: NENNED.[13]

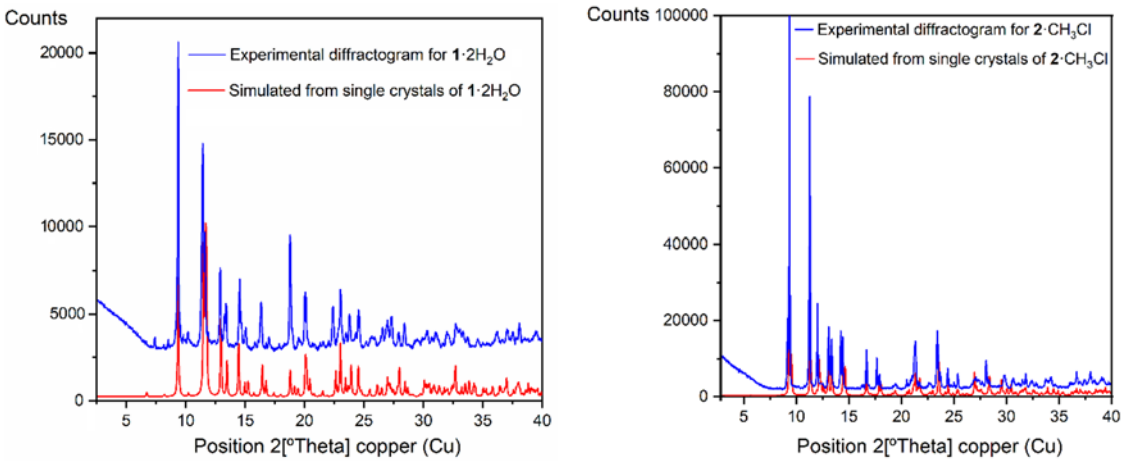

Fig. S4. Comparison of the experimental powder X-ray diffractograms with the corresponding theoretical ones for **1**·$2H_2O$ (left) and **2**·$CHCl_3$ (right)

2. Magnetic Characterization

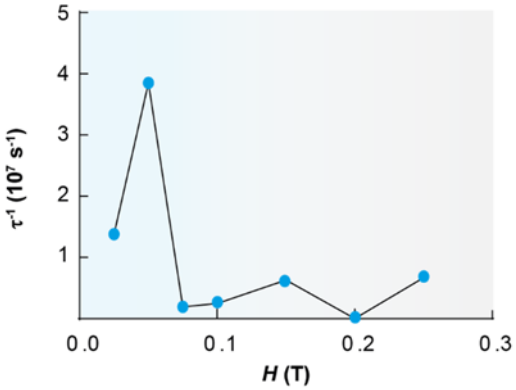

Fig. S5. Dependence of the relaxation time with the field for **1**·2H_2O. The black line is a guide for the eyes.

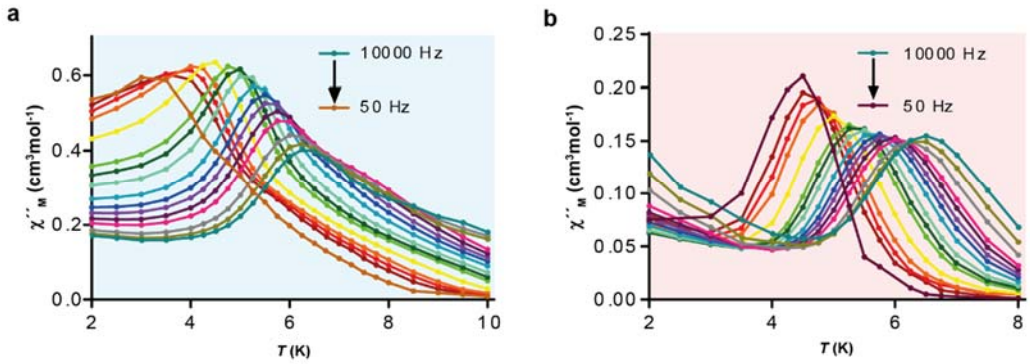

Fig. S6. Temperature dependence of χ_M'' for **1**·2H_2O **(a)** and **2**·$CHCl_3$ **(b)** in a *dc* applied field of 2000 Oe at different frequencies.

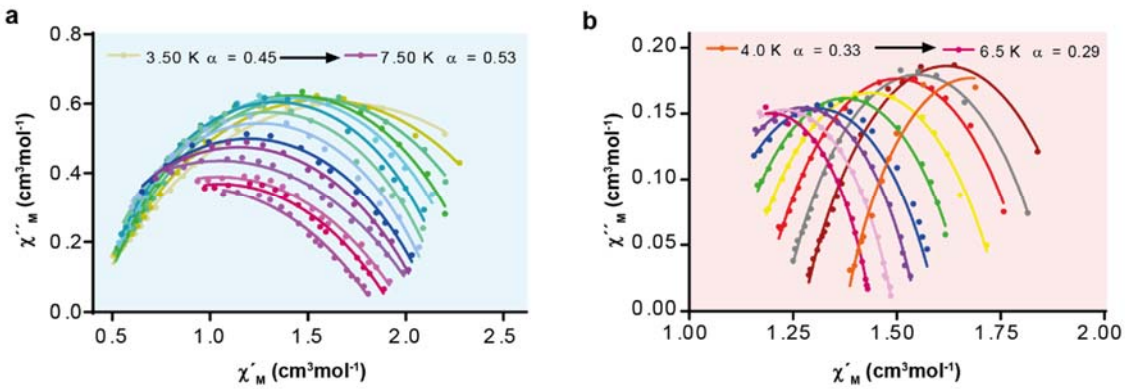

Fig. S7. Cole–Cole plot for **1**·2H_2O **(a)** and **2**·$CHCl_3$ **(b)** in a *dc* applied field of 2000 Oe. In these plots, χ_M'' *vs* χ_M' curves display semicircles for each temperature and can be fitted to the generalized Debye model.[14] The fit provides α parameter values between 1 and 0, and the higher the α value, the larger is the distribution of relaxation times.

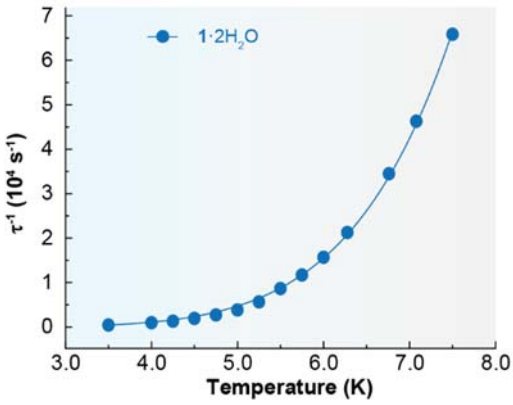

Fig. S8. Dependence of the relaxation time with temperature for **1**·2H_2O in a *dc* applied field of 2000 Oe. The line is the best fit to $\tau^{-1} = CT^n$ (r^2>0.999), i.e. considering only Raman relaxation. Raman parameters: C = 0.13(2) $s^{-1}K^{-n}$ and n = 6.5(1).

3. Photoluminescence Characterization

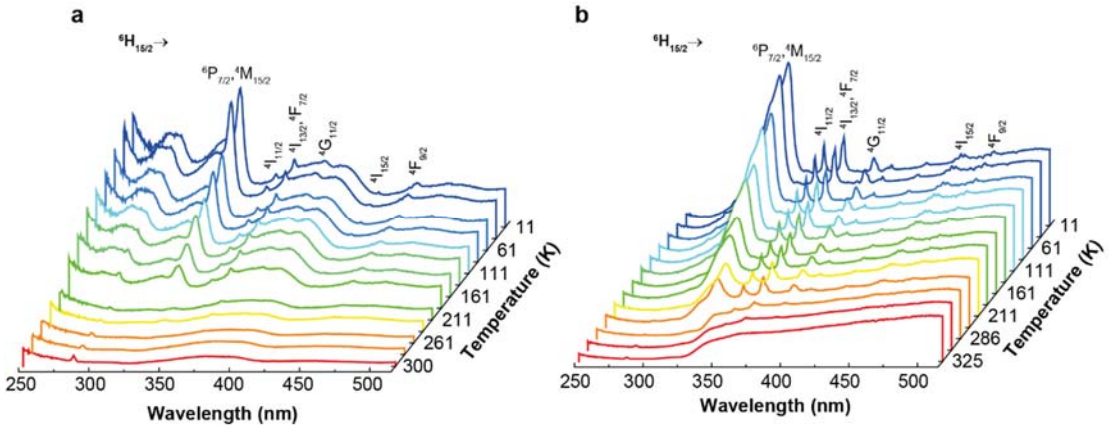

Fig. S9. Excitation spectra of **1**·2H_2O **(a)** and **2**·$CHCl_3$ **(b)** in the 11-325 K temperature range, monitoring the $^4F_{9/2}\rightarrow{}^6H_{13/2}$ transition. The Dy^{3+} transitions are assigned following ref. 15.

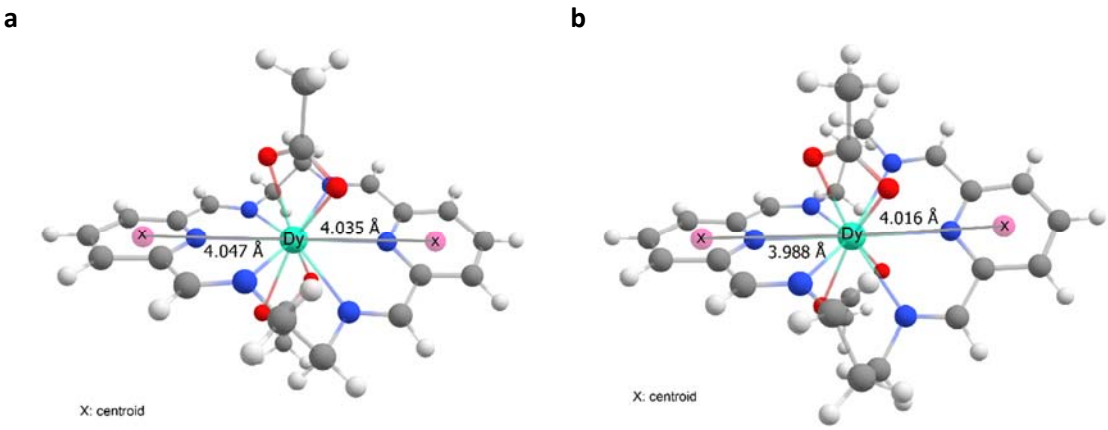

Fig. S10. Distance from the ligand centroid to the Dy^{3+} ion for **1**·2H_2O **(a)** and **2**·$CHCl_3$ **(b)**.

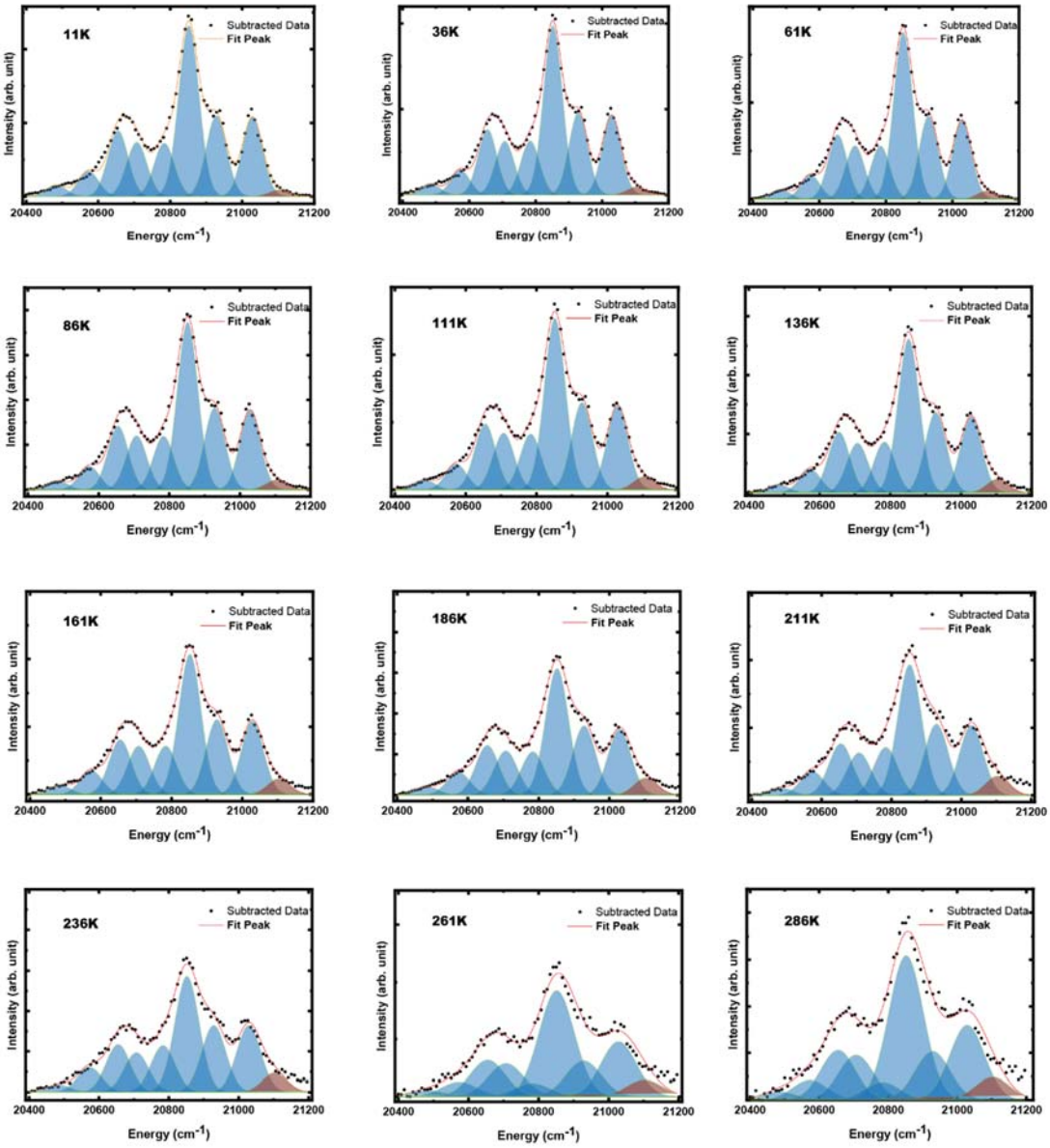

Fig. S11. Emission spectra showing the $^4F_{9/2}\rightarrow{}^6H_{15/2}$ transition for **2**·$CHCl_3$ at different operating temperatures (11-286 K). The spectra were excited at 326 nm. The black circles depict the experimental data, and the red line represents the envelope fit using multi-Gaussian functions. The Gaussian component shadowed in red corresponds to the hot band.

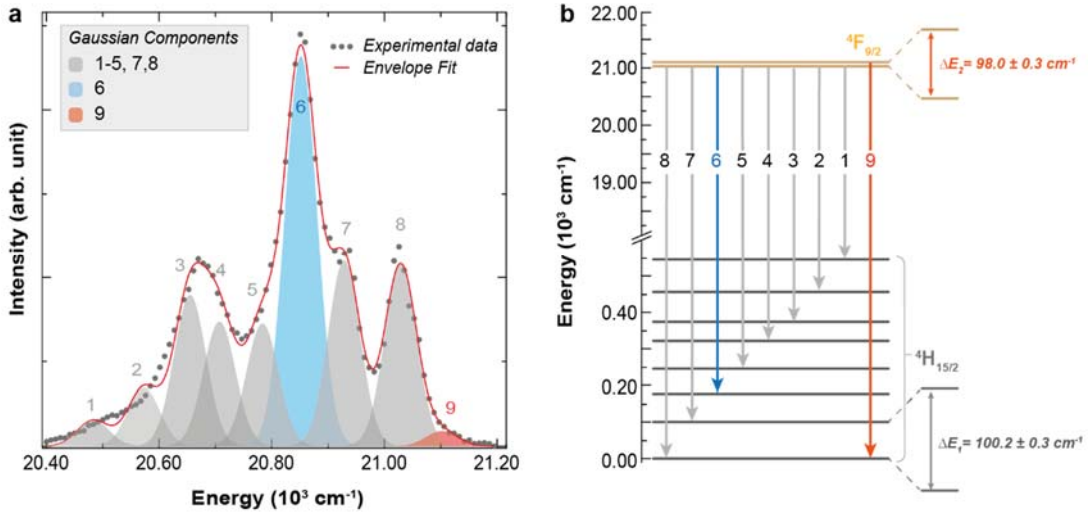

Fig. S12. (a) Deconvolution of the $^4F_{9/2}\rightarrow{}^6H_{15/2}$ transition of **2**·$CHCl_3$ (11 K), excited at 326 nm. The black circles depict the experimental data, and the red line represents the envelope fit using multi-Gaussian functions. The radiative transitions between the first $^4F_{9/2}$ KD and the $^6H_{15/2}$ ones are designated as 1-8, while the Gaussian component labelled 9 corresponds to the hot band (transition between the second $^4F_{9/2}$ KD and the first $^6H_{15/2}$ KD). **(b)** Simplified Dy^{3+} energy diagram estimated from the multi-Gaussian deconvolution of the $^4F_{9/2}\rightarrow{}^6H_{15/2}$ transition in the 11 K emission spectrum of **2**·$CHCl_3$.

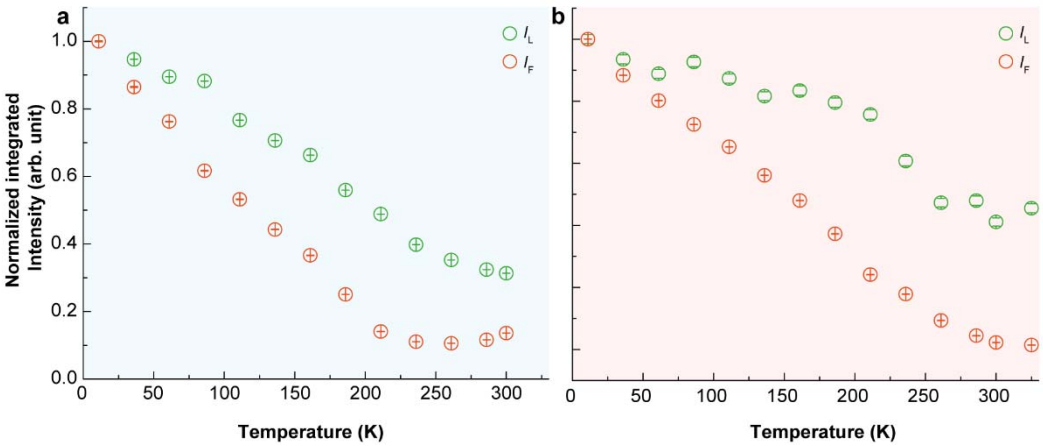

Fig. S13. Normalized integrated intensities of the ligand (I_L) and (I_F) Dy^{3+} $^4F_{9/2}\rightarrow{}^6H_{13/2}$ transitions for **(a) 1**·$2H_2O$ and **(b) 2**·$CHCl_3$.

In **1**·$2H_2O$, the integrated intensity of the ligands decreases steadily until room temperature, while that of the $^4F_{9/2}\rightarrow{}^6H_{13/2}$ transition decreases until 211 K and then remains constant for higher temperatures (Fig. S13). In contrast, for **2**·$CHCl_3$ the integrated intensity of the ligands decreases with temperature until 250 K and then remains constant for higher temperatures, while that of the $^4F_{9/2}\rightarrow{}^6H_{13/2}$ transition decreases until room temperature.

4. Thermometric Characterization

4.1. Secondary thermometers

The secondary luminescent thermometer is based on the ratio of integrated intensities from the ligand and the Dy^{3+} $^4F_{9/2}\rightarrow{}^6H_{13/2}$ transition. The corresponding thermometric parameter is defined as:

$$\Delta = \frac{I_L}{I_F} \qquad \text{(Eq. S1)}$$

where $I_F$is the integrated intensity of the $^4F_{9/2}\rightarrow{}^6H_{13/2}$ transition (resulting from the numerical integration in the 560-590 nm range) and I_L is the integrated area of the ligand emission. The strategy followed to determine I_L is distinct in both compounds: while for **1**·2H_2O is obtained following the normal procedure when we have superposition between different bands by the difference between the numerical integration of the full emission spectra (380-700 nm) and the integrated intensity of the Dy^{3+} $^4F_{9/2}\rightarrow{}^6H_{15/2}$ (470-490 nm), $^4F_{9/2}\rightarrow{}^6H_{13/2}$ (560-590 nm), and $^4F_{9/2}\rightarrow{}^6H_{11/2}$ (653-667 nm) transitions were then subtracted, for **2**·$CHCl_3$ we perform the numerical integration in the 380-470 nm range because there is no superposition. All the numerical integrations were performed in MatLab®.

The corresponding uncertainties in the integrated areas were calculated from the emission spectra evaluating the signal-to-noise ratio. In particular, the uncertainty in each integrated area is determined by evaluating the signal (maximum intensity value for each transition) fluctuations in the emission spectra in the 675-700 nm (**1**·2H_2O) and 500-550 nm (**2**·$CHCl_3$) range (standard deviation, considered as the noise), defining the *SNR=signal/noise* and thus:

$$\delta I_i = \frac{1}{SNR} I_i\,, \qquad i = L, F \qquad \text{(Eq. S2)}$$

The uncertainty in Δ is defined as:

$$\delta\Delta = \Delta \times \sqrt{\left(\frac{\delta I_L}{I_L}\right)^2 + \left(\frac{\delta I_F}{I_F}\right)^2}. \qquad \text{(Eq. S3)}$$

The calibration relations for the secondary thermometers are the straight lines shown in Fig. 7 of the main manuscript described by:

$$\Delta = a \times T + b\,, \qquad \text{(Eq. S4)}$$

where the calibration parameters (a, b) are determined by fitting the experimental Δ values. The fitting parameters are listed in Table S5.

Table S5. Summary of the fitting parameters for the calibration curves of **1**·2H_2O and **2**·$CHCl_3$

Compound	$a\ (K^{-1})$	b	r^2	Operating range (K)
1·2H_2O	-5.0±0.2	(12.7±0.2)×10^2	0.989	11–211
2·$CHCl_3$	-(8.0±0.2)×10^{-3}	2.45±0.05	0.994	11–286

The relative thermal sensitivity (S_r) and the temperature uncertainty (δT) of the secondary thermometers are determined by:16

$$S_r \equiv \frac{1}{\Delta}\left|\frac{d\Delta}{dT}\right| = \frac{a}{a \times T + b}, \qquad \text{(Eq. S5)}$$

and

$$\delta T \equiv \frac{1}{S_r}\frac{\delta\Delta}{\Delta} = \frac{a \times T + b}{a} \times \frac{\delta\Delta}{\Delta}. \qquad \text{(Eq. S6)}$$

4.2. Primary thermometers

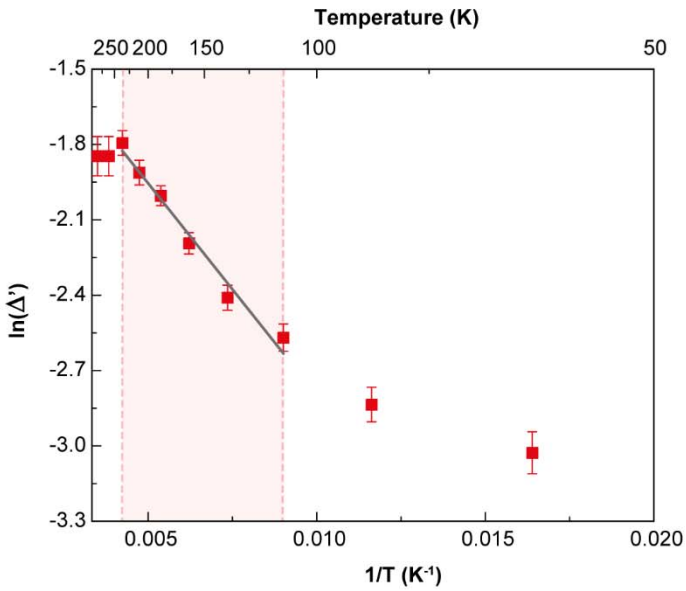

Fig. S14. Plot of the $\boldsymbol{ln(\Delta')}$ with $\mathbf{1/T}$ for **2**·$CHCl_3$. The datapoints follow a linear relation in the shadowed temperature range (86-211 K). The solid line is the best linear fit in the same temperature range (r^2>0.977).

Primary luminescence thermometry exploits the ratio between the intensities arising from two thermally coupled levels (Δ') through a well-established equation, Eq. 2 of the main manuscript. The $\Delta'$is given by:

$$\Delta' = \frac{I_9}{I_6} \qquad \text{(Eq. S7)}$$

where I_6 and I_9 are KDs resulting from the deconvolution of the Dy^{3+} $^4F_{9/2}\rightarrow{}^6H_{15/2}$ transition (Fig. S12 for the labelling of KDs). The I_6 doublet corresponds to the maximum intensity component whereas the I_9 is the "hot band" component.
The uncertainty on Δ' is given by:

$$\delta\Delta' = \Delta' \times \sqrt{\left(\frac{\delta I_6}{I_6}\right)^2 + \left(\frac{\delta I_9}{I_9}\right)^2}, \qquad \text{(Eq. S8)}$$

where $I_6 \pm \delta I_6$ and $I_9 \pm \delta I_9$ are obtained from the deconvolution procedure implemented in OriginLab© software. The intensity value and the corresponding uncertainty are the fitted mean value and its uncertainty, respectively.
The energy difference between the barycenters of the thermally coupled levels (ΔE_2) is determined as $\Delta E_2 = E_8 - E_9$. These values were obtained from the deconvolution procedure, as the barycenter values and the corresponding uncertainties The uncertainty in ΔE_2 results from the E_8 and E_9 uncertainty propagation. The resulting value was ΔE_2=98 ± 0.3 cm^{-1}.

Mean absolute deviation (MAD) is a figure of merit that measures the mean value of the absolute deviation between two datasets. MAD allows the estimation of the accuracy of the measurements[17-21] and is defined as:[21]

$$\text{MAD} = \frac{1}{N} \sum_{\substack{operating \\ range}} |T_c - T_r|, \qquad \text{(Eq. S9)}$$

where the sum extends over the operating range of the primary thermometer, 86 ≤ T_r ≤ 211 K. Fig. S presents the absolute deviation $|T_c - T_r|$ and the MAD values, where r and c label the reference and calculated temperatures, respectively.

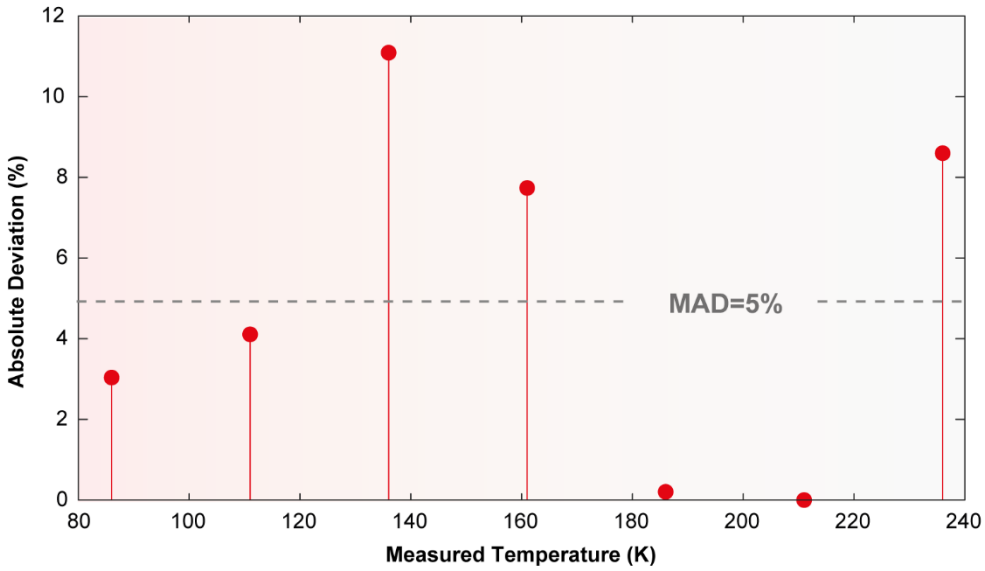

Fig. S15. Absolute deviation $|\boldsymbol{T_c} - \boldsymbol{T_r}|$ in the 86-236 K range for **2**·$CHCl_3$. The $\boldsymbol{MAD}$ is presented as the interrupted line.

The uncertainty on the calculated temperature of the primary thermometer, $\Delta T_c'$, was determined by:[22]

$$\Delta T_c{}' = T_c^2 \sqrt{\left(\frac{\delta T_0}{T_0^2}\right)^2 + \left(\frac{k_B}{\Delta E_2}\right)^2 \left[\left(\frac{\delta \Delta E_2}{\Delta E_2} \ln\left(\frac{\Delta'}{\Delta_0'}\right)\right)^2 + \left(\frac{\delta \Delta_0'}{\Delta_0'}\right)^2 + \left(\frac{\delta \Delta'}{\Delta'}\right)^2\right]} \qquad \text{(Eq. S10)}$$

where $\delta\Delta_0'$ and $\delta\Delta'$ are the uncertainties in Δ_0' and Δ', respectively. The $\Delta T_c'$ values are presented as the error bars in Fig. 9 of the main manuscript.

The performance of the primary thermometer was determined by the S_r and δT values, labelled as $S_r{}'$ and $\delta T'$. $S_r{}'$ is determined by (Fig. S16a):[22]

$$S_r' \equiv \frac{1}{\Delta'}\left|\frac{d\Delta'}{dT}\right| = \frac{\Delta E_2}{k_B T}. \qquad \text{(Eq. S11)}$$

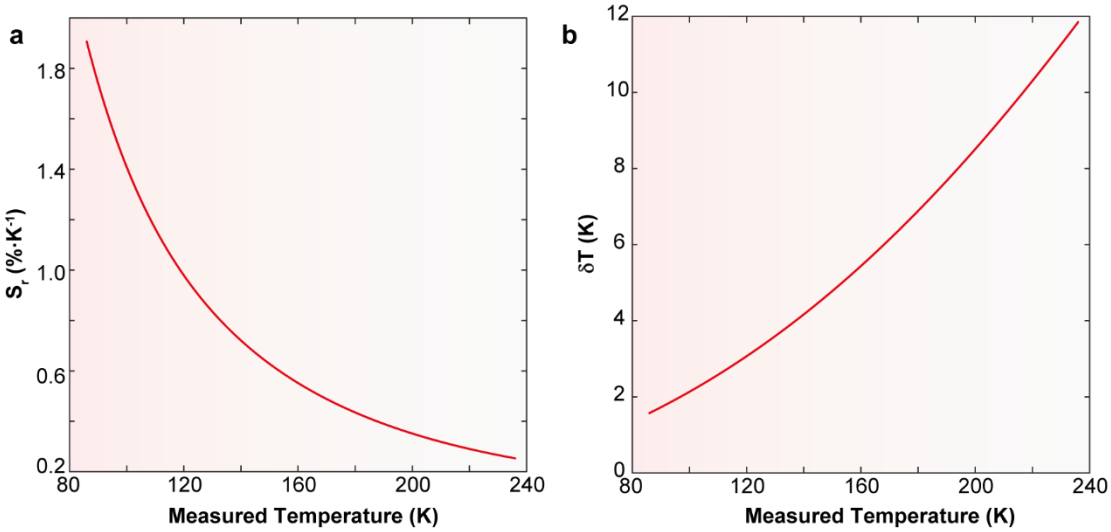

Fig. S16. (a) Relative thermal sensitivity and **(b)** temperature uncertainty of the primary thermometer **2**·$CHCl_3$ in its operating range.

The corresponding temperature uncertainty ($\delta T'$) is determined by (Fig. S16b):[16]

$$\delta T' \equiv \frac{1}{S'_{\mathrm{r}}}\frac{\delta\Delta'}{\Delta'} = \frac{k_B T}{\Delta E_2} \times \frac{\delta\Delta'}{\Delta'} \qquad \text{(Eq. S12)}$$

where $\delta\Delta'/\Delta'$ is the relative uncertainty, determined as 3%.

5. References

1. M. Lee, J. Shim, P. Kang, I. A. Guzei and S. H. Choi, Structural characterization of α/β-Peptides having alternating residues: X-ray structures of the 11/9-helix from crystals of racemic mixtures, *Angew. Chem., Int. Ed.*, 2013, **52**, 12564-12567.
2. T. D. Lash, W. T. Darrow, A. N. Latham, N. Sahota and G. M. Ferrence, Rhodium complexes of carbaporphyrins, carbachlorins, adj-cicarbaporphyrins, and an adj-cicarbachlorin, *Inorg. Chem.*, 2019, **58**, 7511-7526.
3. S. Singh, J. Chaturvedi and S. Bhattacharya, Studies of synthesis, structural features of Cu(I) thiophene-2-thiocarboxylates and unprecedented desulfurization of Cu(II) thiocarboxylate complexes, *Dalton Trans.*, 2012, **41**, 424-431.
4. K. Manoj, R. G. Gonnade, M. S. Shashidhar and M. M. Bhadbhade, Solvent induced crystallization of 1,2,3,4(6),5-penta-O-acetyl-6(4)-O-[(1S)-10-camphor sulfonyl]-myo-inositol diastereomers associated via weak trifurcated C–H⋯O interactions, *CrystEngComm*, 2012, **14**, 1716-1722.
5. T. R. Hayes, B. B. Kasten, C. L. Barnes and P. D. Benny, Rhenium and technetium bi- and tricarbonyl complexes in a new strategy for biomolecule incorporation using click chemistry, *Dalton Trans.*, 2014, **43**, 6998-7001.
6. G. D. Fallon, M. A. P. Lee, S. J. Langford and P. J. Nichols, Unusual solid-state behavior in a neutral [2]catenane bearing a hydrolyzable component, *Org. Lett.*, 2004, **6**, 655-658.
7. W. Harhouri, S. Dhifaoui, Z. Denden, T. Roisnel, F. Blanchard and H. Nasri, Synthesis, spectroscopic characterizations, cyclic voltammetry investigation and molecular structure of the high-spin manganese(III) trichloroacetato meso-tetraphenylporphyrin and meso-tetra-(para-bromophenyl)porphyrin complexes, *Polyhedron*, 2017, **130**, 127-135.
8. O. V. Bykhovskaya, I. M. Aladzheva, D. I. Lobanov, P. V. Petrovskii, K. A. Lyssenko, I. V. Fedyanin and T. A. Mastryukova, Synthesis of 1,2-azaphospholanes containing an amino acid fragment, *Russ. Chem. Bull.,* 2005, **54**, 2642-2647.
9. M. Clemente-León, E. Coronado, M. López-Jordà, J. C. Waerenborgh, C. Desplanches, H. Wang, J.-F. Létard, A. Hauser and A. Tissot, Stimuli responsive hybrid magnets: tuning the photoinduced spin-crossover in Fe(III) complexes inserted into layered magnets, *J. Am. Chem. Soc.*, 2013, **135**, 8655-8667.
10. N. Grabicki, K. T. D. Nguyen, S. Weidner and O. Dumele, Confined spaces in [n]Cyclo-2,7-pyrenylenes, *Angew. Chem., Int. Ed.*, 2021, **60**, 14909-14914.
11. H. Zhou, T. Maris and J. D. Wuest, Using systematic comparisons of 2D and 3D structures to reveal principles of molecular organization. Tetraesters of linear bisisophthalic acids, *J. Phys. Chem. C*, 2012, **116**, 13052-13062.
12. K. Tanaka, K. Hori, S. Tsuyuhara, S. Motoki, S. Shide, R. Arakawa and M. R. Caira, Role of halogen bonding in clathrate formation of tetra- and hexasalicylides derived from halogenated salicylic acids, *Tetrahedron*, 2013, **69**, 1120-1127.
13. A. Peppas, D. Sokalis, D. Perganti, G. Schnakenburg, P. Falaras and A. I. Philippopoulos, Sterically demanding pyridine-quinoline anchoring ligands as building blocks for copper(i)-based dye-sensitized solar cell (DSSC) complexes, *Dalton Trans.*, 2022, **51**, 15049-15066.
14. K. S. Cole and R. H. Cole, Dispersion and absorption in dielectrics I. Alternating current characteristics, *J. Chem. Phys.*, 1941, **9**, 341-351.
15. P. Dharmaiah, C. S. D. Viswanath, C. Basavapoornima, K. V. Krishnaiah, C. K. Jayasankar and S.-J. Hong, Luminescence and energy transfer in Dy3+/Tb3+ co-doped transparent oxyfluorosilicate glass-ceramics for green emitting applications, *Mater. Res. Bull.*, 2016, **83**, 507-514.

16. C. D. S. Brites, A. Millán and L. D. Carlos, in *Handbook on the Physics and Chemistry of Rare Earths*, eds. J.-C. G. Bünzli and V. K. Pecharsky, Elsevier Science, B. V., Amsterdam, 2016, vol. 49, ch. 281, pp. 339-427.
17. P. Bolek, J. Zeler, C. D. S. Brites, J. Trojan-Piegza, L. D. Carlos and E. Zych, Ga-modified YAG:Pr^{3+} dual-mode tunable luminescence thermometers, *Chem. Eng. J.*, 2021, **421**, 129764.
18. D. Manzani, J. F. D. Petruci, K. Nigoghossian, A. A. Cardoso and S. J. L. Ribeiro, A portable luminescent thermometer based on green up-conversion emission of Er^{3+}/Yb^{3+} co-doped tellurite glass, *Sci. Rep.*, 2017, **7**, 41596.
19. R. Alicki and D. M. Leitner, Size-dependent accuracy of nanoscale thermometers, *J. Phys. Chem. B*, 2015, **119**, 9000-9005.
20. E. Ximendes, R. Marin, L. D. Carlos and D. Jaque, Less is more: dimensionality reduction as a general strategy for more precise luminescence thermometry, *Light-Sci Appl*, 2022, **11**.
21. K. M. N. de Souza, R. N. Silva, J. A. B. Silva, C. D. S. Brites, B. Francis, R. A. S. Ferreira, L. D. Carlos and R. L. Longo, Novel and high-sensitive primary and self-referencing thermometers based on the excitation spectra of lanthanide ions, *Adv. Optical Mater.*, 2022, **10**, 2200770.
22. J. C. Martins, A. Skripka, C. D. S. Brites, A. Benayas, R. A. S. Ferreira, F. Vetrone and L. D. Carlos, Upconverting nanoparticles as primary thermometers and power sensors, *Front. Photon.*, 2022, **3**.